Directing the amount of CNTs in CuO–CNT catalysts for enhanced adsorption-oriented visible-light-responsive photodegradation of *p*-chloroaniline

N.F. Khusnun [a], A.A. Jalil [a,b,*], S. Triwahyono [c], C.N.C. Hitam [a], N.S. Hassan [a], F. Jamian [c], W. Nabgan [d], T.A.T. Abdullah [a,b], M.J. Kamaruddin [a,b], D. Hartanto [e]

[a] Department of Chemical Engineering, Faculty of Chemical and Energy Engineering, Universiti Teknologi Malaysia, 81310 UTM Johor Bahru, Johor, Malaysia
[b] Centre of Hydrogen Energy, Institute of Future Energy, Universiti Teknologi Malaysia, 81310 UTM Johor Bahru, Johor, Malaysia
[c] Department of Chemistry, Faculty of Science, Universiti Teknologi Malaysia, 81310 UTM Johor Bahru, Johor, Malaysia
[d] Catalyst Research Division, Research Institute of Petroleum Industry (RIPI), Tehran, Iran
[e] Department of Chemistry, Faculty of Mathematics and Natural Sciences, Institut Teknologi Sepuluh Nopember, Surabaya 60111, Indonesia

ARTICLE INFO

ABSTRACT

Copper oxide (CuO, 10–90 wt%) was loaded onto carbon nanotubes (CNTs) by electrosynthesis method. The catalysts (CuO/CNT) were characterized by XRD, nitrogen adsorption–desorption, ESR, FTIR, Raman, and XPS spectroscopy. The results indicated that a lower amount of CuO was dispersed well on the CNT, while higher loading was agglomerated, producing large-size crystallites, hence resulting in lower specific surface area. Adsorption studies revealed that the isotherms are fitted well with the Langmuir model. Moreover, the n value that was obtained from Freundlich model indicated that adsorption process is chemisorption. Photodegradation of *p*-chloroaniline (PCA) under visible light irradiation demonstrated that the 50 wt% CuO/CNT catalyst gave the highest degradation (97%). It was concluded that C—N moieties of PCA were chemisorbed on the catalyst prior to photodegradation, while the Cu—O—C bonds, surface defects and oxygen vacancies were the main active site in enhancing the subsequent photodegradation. The kinetics of photodegradation were correlated with pseudo-first-order model, verifying the surface reaction was the controlling step. Remarkable mineralization results of PCA were attained by TOC (89.1%) and BOD_5 (50.7%). It was also evidenced that the catalyst has a good potential toward degradation of various endocrine disruption compounds.

© 2017 Elsevier B.V. All rights reserved.

1. Introduction

p-Chloroanilines (PCAs) are common water pollutants which are used as intermediates in the plastics, defense, paint, printing, pesticide, and pharmaceutical industries, as ensured by its existence in sludge, agricultural soil and industrial effluent [1–4]. Thus, various treatment technologies have been reported to eliminate this persistent organic pollutant from such wastes, based on different processes and reagents [4–8]. However, their uses are limited by several disadvantages such as high material and operational cost, the production of secondary wastes, as well as their time-consuming natures.

Over the past three decades, advanced oxidation processes (AOPs) have gained increasing attention as promising benign environmental processes for the elimination of organic or inorganic contaminants in water and wastewater [9]. However, incomplete mineralization and

non-selective target pollutants, as well as inappropriate operating conditions have prompted their combination with other AOPs such as photocatalysis, the addition of H_2O_2 or membrane technologies [10]. In fact, heterogeneous photocatalytic degradation is a popular and an economical process that converts the pollutants to the less harmful final products, which are carbon dioxide and water [11]. Besides TiO_2, there are many photocatalysts or a hybridization of two that have been reported, including SnO_2, ZnO-CeO, Fe_2O_3-TiO_2, ZnS, ZnO–MSN, and AgO–TiO_2 [12–16]. The use of mesoporous materials such as silica, zeolite and alumina as supports for TiO_2 is also among the efforts to lower the band gap, as well as to suppress the fast electron–hole recombination rate [17–19].

Recently, the unique properties such as excellent electron conductivity, superior mechanical and thermal stability, high surface area and well-defined hollow interiors have encouraged many researchers to use carbon nanotube (CNT) as photocatalyst [20]. The loading of CNTs onto metal oxides such as ZnO, TiO_2, Fe_3O_4, and Al_2O_3 is able to alter the physicochemical properties of the catalysts, and enhance the photocatalytic degradation of organic pollutants [21]. However, the investigations generally focus on the low CNT amounts, which is below 20%. The

high cost and dark color of CNTs are most probably the main constraints to use high amounts of CNT photocatalyst. Nevertheless, due to the high demand of CNTs, particularly for other commercial applications, a large-scale production is developed by various synthetic methods, and a cost-effective production from wastes has become a popular route nowadays [22]. A large-scale production has been defined as the production of 10,000 tons of CNTs per annum [23]. Hence, for those reasons, in addition of the fewer work on the use of high CNT loading amounts in photocatalysts, we report herein for the first time the effect of a full range of CNT contents and their photocatalytic activity. A narrow-band-gap CuO (1.2–1.5 eV) was coupled with CNTs in order to alter the electronic band gap of the hybrid catalysts and shift the absorption spectrum toward the visible light region [24]. The catalysts were characterized by XRD, N_2 adsorption–desorption, ESR, FTIR, Raman and XPS. The detailed adsorption–photocatalytic performance in the degradation of p-chloroaniline (PCA), kinetic studies, and the mechanism of degradation are also discussed. In fact, there have been only a few reports on the degradation of PCA via basic AOPs, including the use of ozone, photoinduced iron (III), and persulfate activated with zero-valent iron [6,25,26]. The outcomes from this report are believed could contribute to the design of superior CNT-based catalysts for numerous use.

2. Experimental

2.1. Material

All chemicals used in this study were analytical grade and were used without further purification. Only tetraethylammonium perchlorate (TEAP) was prepared by previous reported method [27].

2.2. Synthesis of catalysts

The CuO/CNT catalysts were synthesized by electrolysis preparation method in accordance with the procedure that was described in previous study [28]. The only difference is the amount of copper content on the CNT which are in the range of 10 to 90%. The as-synthesized catalysts were ready to be used for further analysis and testing.

2.3. Characterization

X-ray diffraction (XRD) patterns were collected to detect the crystallinity of the catalyst by X-ray diffractometer executed on a Bruker Advance D8 X-ray equipped with a Cu-Kα characteristic radiation source at 2 theta angle ranging from 20° to 80° with a step size of 1°min^{-1}. The morphology structure of catalyst was characterized by Transmission Electron microscopy (TEM) using JEOL JEM-2100F microscope. The samples were ultrasonically dispersed in acetone and deposited on an amorphous and porous carbon grid. Nitrogen physisorption at 77 K using a SA 3100 Beckman Coulter Surface Analyzer was performed to determine the structural properties (i.e., specific surface area, pore volume, and pore diameter). In order to confirm the functional group of CuO/CNT, Fourier transform infrared (FTIR) spectra were recorded using a Perkin Elmer Spectrum GX FTIR spectrometer in the range of 4000–400 cm^{-1} using a KBr pellet method. The electronic structure of the catalyst were identified by JEOL JES-FA100 Electron Spinning Resonance (ESR) spectrometer. X-ray photoelectron spectroscopy (XPS) conducted on a Kratos Ultra spectrometer equipped with a Mg K α radiation source (10 mA, 15 kV) in the range of 0–800 eV were used to investigate the Cu state. Raman spectra were conducted on a Jobin Yvon Horiba HR800 spectrometer using a 532 nm line of Nd ion laser as excitation source at room temperature.

2.4. Photodegradation of PCA

The degradation performance of PCA by all catalysts were conducted under similar condition with previous research [28]. However, in this study, the reaction was performed for only 3 h under visible light (VL)

irradiation using a batch reactor fixed with a metal halide lamp (4 × 400 W; 400 nm emission). After irradiation for varying periods of time, aliquots of the solution were taken and centrifuged in a Beckman Coulter Microfuge 16 centrifuge at 14000 rpm for 10 min. The amount of PCA remaining in solution was determined by UV–vis spectroscopy using an Agilent Technology Cary 60 UV–Vis spectrophotometer. The maximum adsorption peak at 239 nm was used to measure the PCA degradation. The regeneration of the catalyst toward PCA degradation was carried out by a repeated experiment over 50 wt% CuO/CNT to study its stability. After each reaction, the solution were centrifuged, and the separated catalyst was calcined before it to be used in the subsequent reactions. Moreover, the samples before and after reaction were then analyzed for total organic carbon (TOC) content on TOC Shimadzu V_{cph} spectrophotometer, while biological oxygen demand (BOD_5) determinations were carried out according to the Standard Methods (5120) by the OxiTop® procedure.

3. Results and discussion

3.1. Structural properties of catalyst

Fig. 1A shows the wide-angle XRD pattern of electrosynthesized CuO, while CNT and copper (0–90 wt%)-loaded CNT (CuO/CNT) catalysts in the range of 2θ = 20–80° are shown in Fig. 1B. The electrosynthesized CuO nanoparticles showed characteristic peaks for the pure monoclinic structure of CuO (JCPDS 48–1548) at 32.5°, 35.5°, 38.7°, 48.8°, 53.4°, 58.2°, 61.5°, 65.8°, 67.9°, 72.4°, and 75.11°, which corresponded to (110), (002), (111), (202), (020), (202), (113), (311), (113), (311), and (222) planes, respectively [26,29]. The CNT showed two main peaks at 2θ = 25.7° (002) and 42.9° (100), attributed to the structural ordering of CNTs [30]. The introduction of copper notably decreased the intensity of these peaks, and diffraction peaks corresponding to the CuO increased with the increasing Cu loading. No peaks corresponding to CNT were observed in the 90 wt% CuO/CNT; this may be due to the highest amount of CuO covering the diminutive amount of CNT [31]. The crystallite size of CuO was estimated using the Scherrer equation based on the most intense peak at 35.5° and the values are listed in Table 1. It was seen that the crystallite size of the CuO was larger than the CuO in the CuO/CNT catalyst, suggesting the latter was well dispersed on the CNT surface [32].

Next, further investigation on morphology of the 50 wt% CuO/CNT catalyst was examined by TEM and the images are shown in Fig. 1C and D. It could be seen from Fig. 1C that the tube-shaped materials is confirmed to be CNT and the dark regions with the crystallite size <20 nm are CuO nanoparticles. The lattice d-spacing of nanocrystals were examined and as shown in Fig. 1D, the region marked by white lines with a value of 0.242 nm should be the (1 1 1) plane of the CuO structure [33]. While, the area marked by black line with a d-spacing of 0.4 nm could be indexed as the (0 0 2) plane of CNT [20].

Nitrogen adsorption–desorption isotherms and the corresponding pore size distribution plots of all catalysts are shown in Fig. S1, while their thorough structural properties are tabulated in Table 1. An inset figure in Fig. S1A shows the pristine CNT possessed a type II isotherm with no hysteresis loop (IUPAC classification); this seems to be due to its smooth inner walls [34,35], while both CuO and CuO/CNT catalysts showed a type IV profile and H3 hysteresis loops (Fig. S1A/a–c), representing the characteristics of mesoporous materials with slit-shaped pores of non-uniform size and/or shape [36]. Although the isotherm types are quite similar, their pore structures are somewhat different. For the catalyst with a larger amount of CNTs (Fig. S1A/a-b), a sharp increase in nitrogen uptake was observed at relative pressure P/Po = 0.6–0.99, demonstrating that the 10 wt% and 50 wt% CuO/CNT have larger interparticle pores than the others [37]. This was clarified by their pore size distribution, which was analyzed by the NLDFT method shown in Fig. S1B and its enlarged version in Fig. S1C. It was seen that almost all the larger pores (>10 nm) in the CNT were decreased
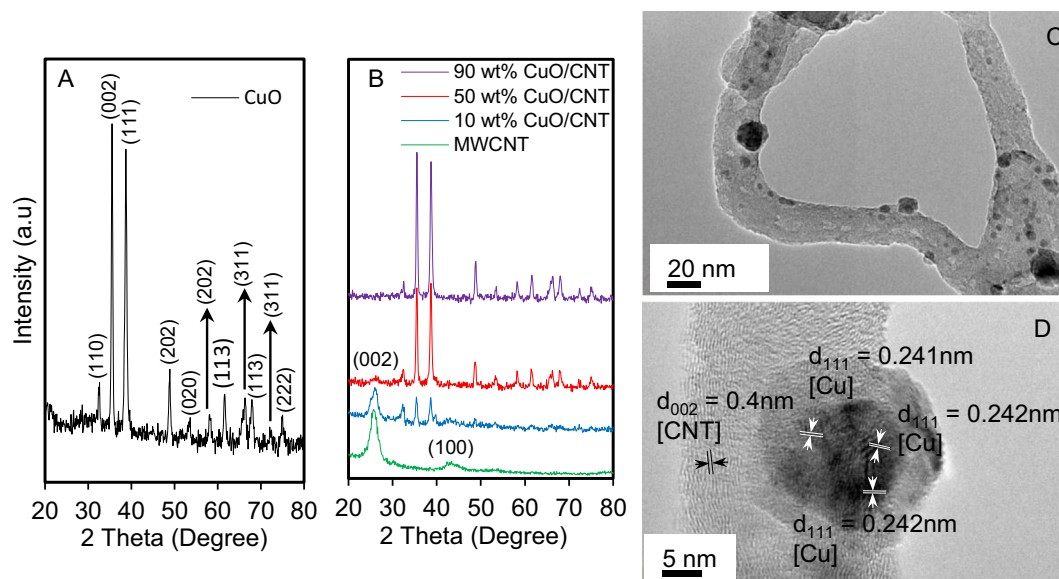
Fig. 1. XRD pattern for (A) CuO and (B) synthesized catalyst; TEM images of 50 wt% CuO/CNT catalyst at (C) low magnification and (D) high magnification.

considerably by the introduction of CuO (Fig. S1B), and the smaller pores were blocked progressively by the increasing amount of CuO. A similar trend was observed with the decrease in total pore volume and surface area, as listed in Table 1. This result was in match with the XRD result, where the higher the amount of CuO, the larger the crystallite size of the CuO covering the surface of CNT, thus reduced its crystallinity.

3.2. Chemical properties

To verify the interaction between copper and CNT, the CuO/CNT catalysts were then examined by FTIR spectroscopy, and the spectra in the region of 4000–400 cm^{-1} are shown in Fig. 2A. All catalysts exhibited five main bands at 3432, 2919, 1595, 1095–1030, and 536 cm^{-1}, which are attributed to O—H stretching, C—H stretching, C=C cyclic alkene vibration, C—C and C—O vibration from TEAP, and Cu—O vibration, respectively [38]. Magnification of the band at 536 cm^{-1} (Fig. 2B) showed that its intensity decreased considerably when >50 wt% of CNT was introduced, signifying that the structure of the CuO/CNT catalysts was extremely perturbed by the large amount of the CNT. For detailed investigation, the band at 536 cm^{-1} was plotted by Gaussian curve fitting. As seen in Fig. S2, the band is fitted to four bands at 582, 536, 480, and 430 cm^{-1}. The first three bands are due to the monoclinic phase, and can be assigned to the Cu—O stretching vibration along the (101) direction [33,39], while, the bands at 480 and 430 cm^{-1} can be also assigned to the Au and Bu modes of Cu—O vibrations, respectively [40]. Notably, a new band arose at 512 cm^{-1} when CNT was hybridized with CuO, verifying that both interacted to form Cu—O—C bonds [28]. For a detailed comparison, the intensities of those bands are summarized in Fig. 2C. It was seen that generally all the bands in pristine CuO become more pronounced by the introduction of 10 wt% of CNT, with the emergence of the new band of Cu—O—C, indicating the CuO had now interacted with the CNT [41].

This is also an evidence of the successful formation of the CuO-CNT nanocomposite through electrostatic interactions. The 50 wt% CuO/CNT possessed the highest intensity of Cu–O–C band, demonstrating its high potential as photocatalyst among the others [28], while all the CuO bands weakened when the CNT became dominant.

Next, ESR spectroscopy was used to clarify the electronic structure of the catalysts with unpaired electrons (Fig. 3A). Pure CNT showed a g-value = 2.01 (inset figure), which is similar with the result obtained by other studies [42]. Its strong ESR signal indicated the presence of defect sites, as well as abundant unpaired electrons, which arose from defects or open tips in the lattice of nanotube [43]. The g-value of the pure CuO was found to be 1.88, indicating its electron-deficient state, but hybridization with CNT shifted its ESR resonance to 2.00 which reflected the decreasing internal magnetic field in the vicinity of the ordered state, denoting charge compensation by the new species [44]. The shift in the g-value could be associated with the change in the environment of Cu^{2+}, or with other obscuring factors, such as spin state, coordination geometry and nature of the donors [45]. In addition, the broad ESR signal clearly indicates the presence of a large number of defects in the CuO including Cu^+ or oxygen vacancies (V_o). The signal intensity of both pristine CNT and CuO was obviously decreased due to hybridization, particularly for the former, which signified the main reduction of defect sites occurred on the CNT backbones [46]. This result supported the FTIR and XRD data, confirming the perturbation of the CNT structure by the introduction of CuO or vice versa.

Raman spectra were then used to determine the microstructural characteristics of the modified CNTs. As seen in Fig. 3B, two common bands for CNT were observed at 1352 cm^{-1} (D band) and 1580 cm^{-1} (G band), which are associated to the structural defects/disordered of sp^2 domain and the E_{2g}-vibration mode of sp^2 hybridized carbon-based materials, respectively [47]. Commonly, the intensity ratio (R = I_D / I_G) value of the D-band to G-band is considered for evaluating the structure alterations of the CNT. As exhibited in Fig. 3B, the calculated R value increased from 1.27 for pristine CNT to 1.47 for 10 wt% CuO/CNT, which is related to the fact that introduction of CuO onto the CNT causes significant surface structural defects [48]. However, further addition of CuO to 50 wt%, decreased the R value, this most probably due to the Cu—C interaction that led to fewer structural defects. However, larger amounts of CuO gave no peaks for both bands, indicating the diminutive amount of CNT in the catalyst. These results are also in agreement with the FTIR data, particularly where the 50 wt% CuO/CNT possessed the greatest number of Cu–O–C bonds.

Table 1
Structural properties of the catalysts.

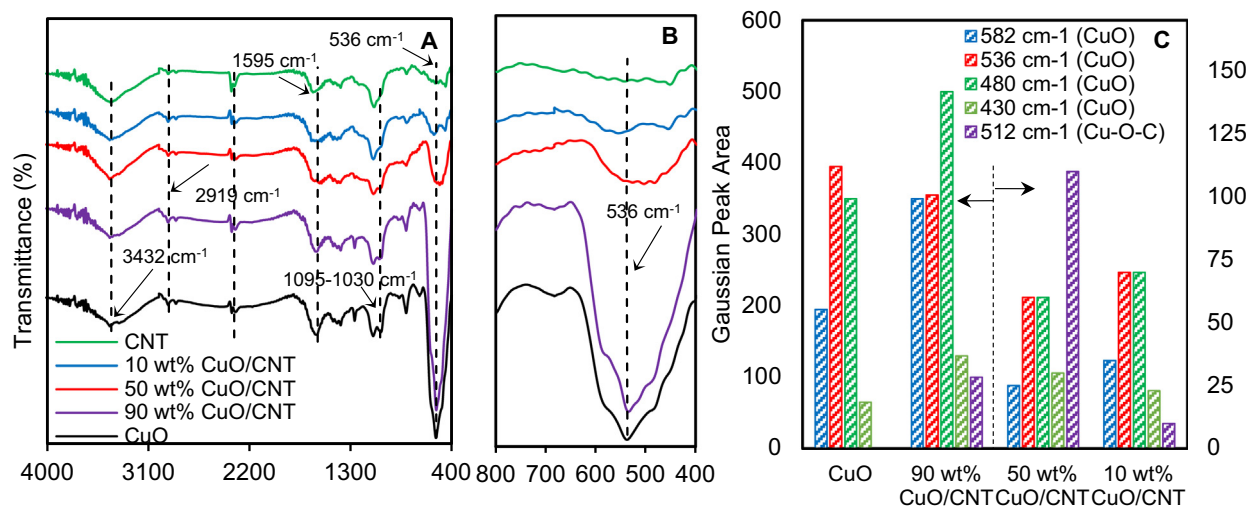| Catalysts	Surface area (S_{BET})	Pore volume	Pore size (nm)	Crystallite size[a] (nm)
CuO	2.54	0.01	7.32	26.5
90 wt% CuO/CNT	5.86	0.03	6.08	19.9
50 wt% CuO/CNT	64.4	0.11	5.09	17.9
10 wt% CuO/CNT	176	0.21	6.08	15.9
CNT	181	0.79	52.4	–

[a] Calculated by Scherer equation.

Fig. 2. FTIR spectra at the range of (A) 4000–400 cm^{-1} (B) 800–400 cm^{-1} (C) intensities of deconvoluted peak at range 800–400 cm^{-1}.

The 50 wt% CuO/CNT was also analyzed by XPS in order to determine its chemical properties and the spectra are shown in Fig. 3C. The binding energies at around 935.4 and 962.31 eV are corresponds to Cu 2p$^{3/2}$ and Cu 2p$^{1/2}$ peaks, respectively. In addition, there are two peaks at 942.0 and 952.7 eV, indicating the Cu^{2+} species of CuO [49]. Another peaks were detected at 933.1 and 952.7 eV which belongs to Cu 2p$^{1/2}$, signifying the existence of reduced copper species Cu^{+}, which prove the presence of C–O–Cu^{+} defect or V$_o$ as discovered in the FTIR and ESR data.

3.3. Performance activities

3.3.1. Adsorption equilibrium and kinetics studies

Generally, the adsorptions were performed for each catalyst under dark condition prior to photocatalytic reaction. The isotherms and adsorption parameters (q_{max}, K_L, K_F, n, and R^2) of the catalysts for adsorption of PCA are displayed in Fig. 4A and Table 2, respectively. All catalyst equilibrium times were achieved at 120 min and the adsorption percentage toward 10 mg L^{-1} PCA were 7.69, 4.93, 2.59, 1.41 and 0.95 mg g^{-1} when using CNT, 10 wt% 'CuO/CNT, 50 wt% CuO/CNT, 90 wt% CuO/CNT, and CuO, respectively. It was seen that the higher amount of CNT offered a higher adsorption percentage, undoubtedly due to its inherently larger surface area. The fitting of the data to the linear plots of Langmuir (Fig. S3/A–E) and Freundlich (Fig. S3/F–J) models

resulted in the highest R^2 of the former model (0.97–0.99), signifying a monolayer adsorption, in which there is no transmigration of the adsorbate on the surface plane [36]. Moreover, due to higher R^2 (0.92–0.97) of latter isotherms, it also could be considered in explaining the nature and mechanism of the adsorption due to their parameter values. The heterogeneity factor (n) is used to identify the adsorption, i.e. whether it is linear (n = 1), a chemical process (n < 1) or a physical process (n > 1). The n values that were obtained in this study are 0.46, 0.61, 0.53, 0.44, and 0.77 for CNT, 10, 50, 90 wt% CuO/CNT and CuO, respectively. These values are clarified as a chemisorption process, most probably associated with the attraction of the PCA toward the hydroxyl and carboxyl groups and/or π-π bonds on the CuO/CNT [21].

The adsorption kinetics were carried out to examine the adsorbate uptake rate and also to propose an adsorption mechanism. Herein, the experimental data were fitted to two conventional linear kinetic models; namely the Lagergren pseudo-first-order model and the Ho pseudo-second-order model. Lagergren's first-order rate equation describes the adsorption rate based on adsorption capacity and the equation is as follows:

$$\ln (q_e - q_t) = \ln q_e - K_1 t \tag{1}$$

where q_e is the amount of PCA adsorbed (mg g^{-1}) onto the adsorbent at equilibrium, q_t is the amount of PCA adsorbed (mg g^{-1}) onto the
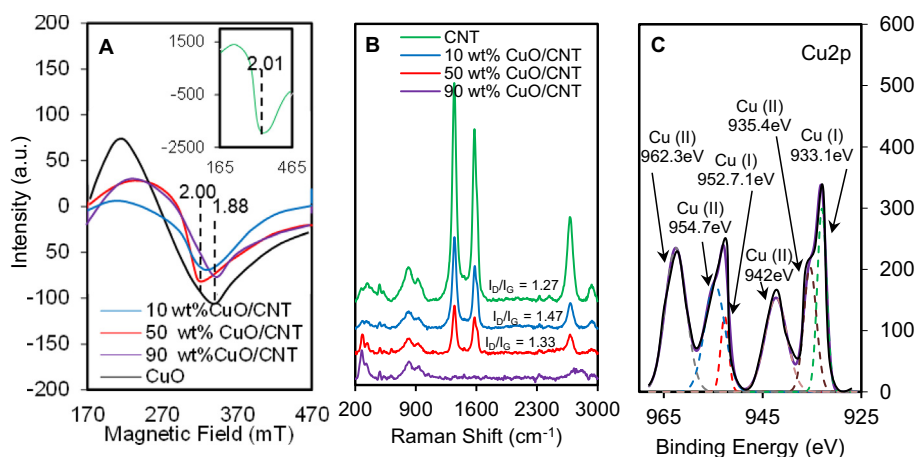

Fig. 3. (A) ESR spectra of CNT (inset figure) and all catalysts (B) XPS spectra of Cu 2p for 50 wt% CuO/CNT (C) Raman spectra of the catalysts.
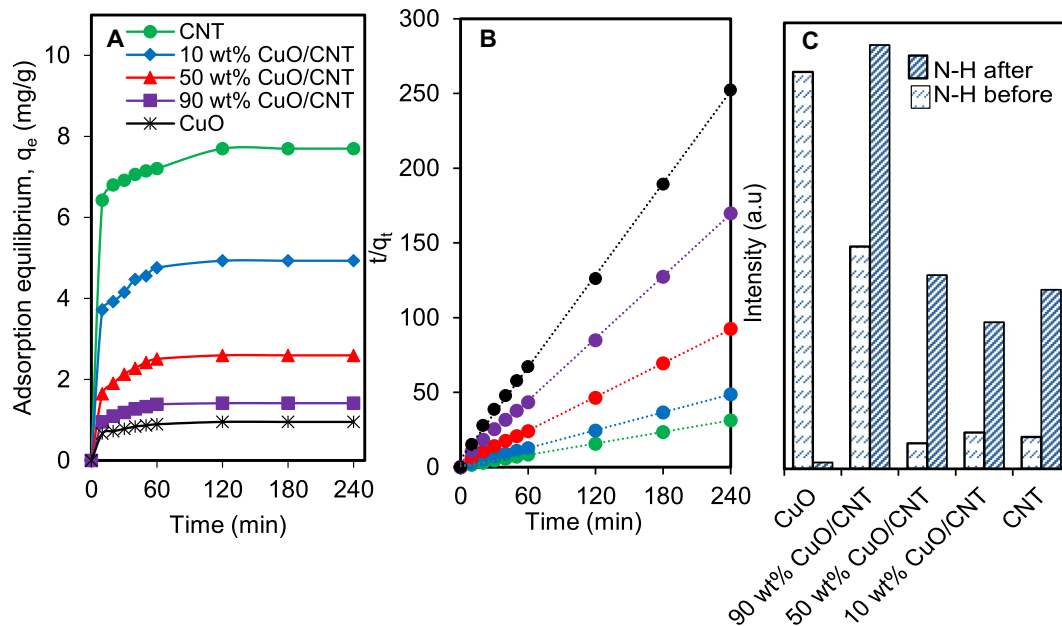
Fig. 4. (A) Adsorption of PCA over all samples (B) pseudo-second order adsorption plot (C) summary of C—N stretching vibration intensity from FTIR before and after the adsorption of PCA.

adsorbent at any time t, and K_1 (min^{-1}) is the rate constant of the pseudo-first-order adsorption which can be calculated from the slope of the linear plot of ln $(q_e - q_t)$ vs. t. The linearized equation of the Ho pseudo-second order model is as follows:

$$\frac{t}{q_t} = \frac{1}{K_2 q_e^2} + \frac{1}{q_e} t \qquad (2)$$

where K_2 is pseudo-second-order rate constant (g mg^{-1} min^{-1}), which can be calculated from the slope and intercept of the plot of t/q_t against t, while other parameters are the same as above. As shown in Fig. 4B, all the points are best fitted with pseudo-second-order kinetics compared to pseudo second-order model (figure not shown), and the corresponding regression coefficient values (R^2) for the former are all closer to unity (Table 3), suggesting that adsorption is better represented by this model [50,51]. This result could indicate that the adsorption occurs through a chemisorption process [36], which would involve the interaction between either the —NH$_2$ group from the PCA with the —OH and —COOH of CNT or between the benzene ring of the PCA with the carbon groups of CNT via π-π interaction [21]. This is in agreement with the nature of the adsorption above where the process was co-operative adsorption.

The adsorption of PCA onto the catalysts was further confirmed by the FTIR spectra of the fresh and spent CuO/CNT. The magnification of the band at 1257 cm^{-1}, which is attributed to the C—N stretching

vibration is shown in Fig. S4 [52], and the summary of its intensity for each catalyst are shown in Fig. 4C. In fact, the C—N group detected before the adsorption on the catalysts, particularly on the CuO and 90 wt% CuO/CNT, was supposed to originate from the TEAP electrolyte, which was consumed during the preparation of the catalysts. It was clearly observed from Fig. 4C that the PCA was adsorbed by the all CNT-based catalysts.

3.3.2. Photocatalytic testing and kinetics studies

The photodegradation of PCA for all catalysts was then tested as shown in Fig. 5A. It can be clearly observed from Fig. 5A that under optimum pH 7 (Fig. S5A), using 0.375 g L^{-1} catalyst dosage (Fig. S5B), the photocatalytic efficiency was in the following order: CuO (75.5%) < 90 wt% CuO/CNT (82.1%) < CNT (84.7) < 10 wt% CuO/CNT (91.8%) < 50 wt% CuO/CNT (97.0%). Significantly, hybridized 50 wt% CuO/CNT catalysts could enhance the degradation percentage up to 97%, demonstrating the important role of both materials in the reaction. The adsorption of PCA also seems to facilitate the photodegradation.

For detailed investigation, the kinetics of the degradation were investigated by applying the Langmuir-Hinshelwood (L–H) model modified to accommodate reactions occurring at a solid–liquid interface [53]. In this study, a sequence of run using various initial PCA concentrations ranging from 10 to 100 mg L^{-1} were carried out under UV–vis irradiation and the results are shown in Fig. 5B. The model is expressed by the simplified equation as follows:

$$\ln\left(\frac{C_0}{C}\right) = kt \qquad (3)$$

Table 2
Langmuir and Freundlich equilibrium models for adsorption of PCA.

Photocatalyst	Langmuir			Freundlich		
	q_{max}	K_L	R^2	n	K_f	R^2
CNT	31.1	0.052	0.998	0.46	3.62	0.935
10 wt% CuO/CNT	32.7	0.023	0.989	0.61	1.55	0.974
50 wt% CuO/CNT	11.7	0.036	0.974	0.53	0.92	0.921
90 wt% CuO/CNT	4.88	0.048	0.995	0.44	0.60	0.933
CuO	12.0	0.009	0.977	0.77	0.17	0.997

q_{max} is the maximum adsorption capacity (mg g^{-1}).
K_L is the Langmuir constant (L mg^{-1}).
K_F is the adsorption equilibrium constant (mg g^{-1} (mg L^{-1})$^{-n}$).
n is a constant indicative of adsorption intensity.
R is correlation coefficients.

Table 3
Adsorption kinetics for PCA.

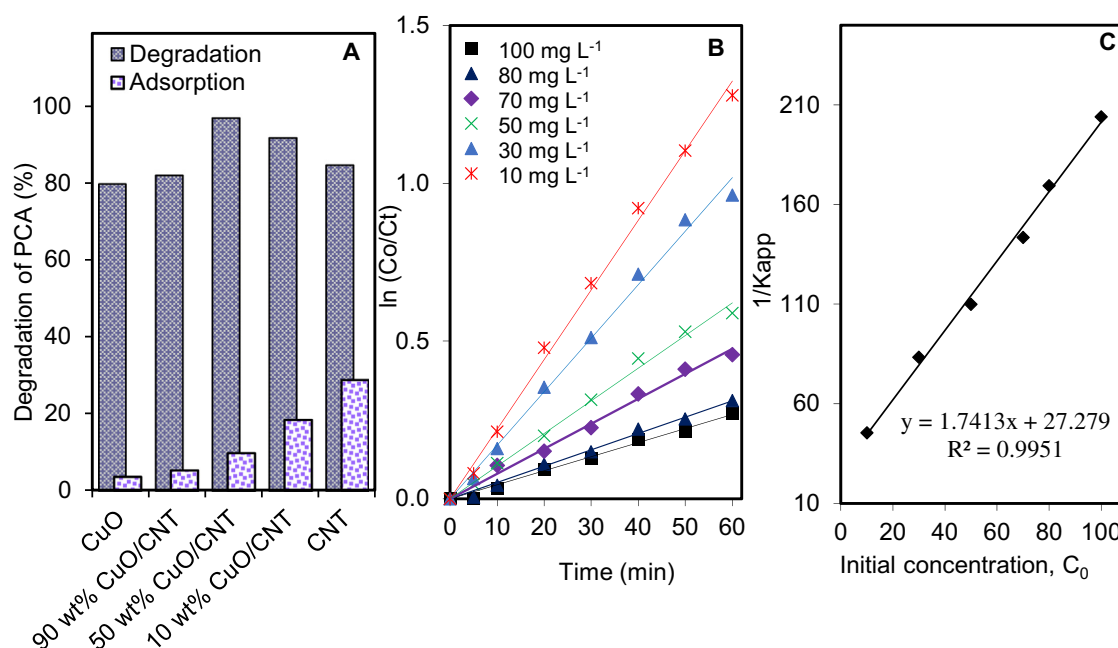| Photocatalyst	First-order			Second-order		
	q_e	K_1	R^2	q_e	K_2	R^2
CNT	3.07	0.037	0.703	7.79	0.044	0.999
10 wt% CuO/CNT	3.10	0.047	0.921	5.02	0.052	0.999
50 wt% CuO/CNT	2.10	0.051	0.977	2.66	0.075	0.999
90 wt% CuO/CNT	1.13	0.057	0.960	1.44	0.124	0.999
CuO	1.61	0.041	0.930	0.97	0.205	0.999

Fig. 5. (A) Adsorption and photodegdradation of PCA over all catalysts (B) kinetics study under different initial concentration (C) relationship of k_{app} with initial concentration.

where k is the pseudo-first-order rate constant and C_0 and C_t are the concentrations of PCA at initial time and time t, respectively. A significant effect of CuO/CNT catalysts on the photodegradation of PCA was revealed by the k values listed in Table 4. From the linearity of the plot of ln (C_0/C_t) vs. irradiation time t, it was clear that the photodegradation obeyed approximately the pseudo-first-order kinetics model, implying that the richness of PCA on the catalyst surface suppressed the photodegradation percentage. Rahman et al. also found the same finding when investigating the effectiveness of γ-Fe$_2$O$_3$ embedded PVA–alginate beads in removal of Hg (II) using photocatalytic process [54]. In addition, the L–H kinetic model was plotted (Fig. 5C) based on the following equation:

$$\frac{1}{k_{app}} = \frac{1}{k_r k_{LH}} + \frac{C_0}{k_r} \tag{4}$$

where k_{app} is the apparent rate constant, k_r is the reaction rate constant (mg L^{-1} min^{-1}) and k_{LH} is the adsorption coefficient of the reactant (L mg^{-1}). From the slope and intercept of the line, the values of k_r and k_{LH} were calculated to be 0.5743 mg L^{-1} min^{-1} and 0.0638 L mg^{-1}, respectively, demonstrating that the PCA adsorption was the controlling step of the process. This result resolved the substantial task of determining the mechanism of adsorption in this photodegradation. Similar kinetic studies were reported by Feng et al. and Shen et al. who studied the adsorption and photocatalytic degradation of Rhodamine B over a reduced graphene oxide-ZnFe$_2$O$_4$-based catalyst [55,56].

3.4. Proposed mechanism of photodegradation

Accordingly, the 50 wt% CuO/CNT catalyst was chosen for next determination on the mechanism of PCA degradation. Three scavenging agents were used in order to identify the key factors in the reaction: sodium oxalate, potassium peroxodisulphate, and sodium bicarbonate, which act as hole capturer (h$^+$), electron trapper (e$^-$), and surface hydroxyl radical scavenger (•OH$_{surf}$), respectively [29]. As shown in Fig. 6A, the order of those key factors is as follows: e$^-$ < •OH$_{surf}$ < h$^+$. Thus, based on these and all results above, the photodegradation mechanism of PCA is proposed as follows. The visible light irradiation causes photogenerated electrons on the CuO and CNTs to be transferred to their conduction band (CBs), leaving holes at their valence band (VB) (Eq. (5)) [57,58]:

$$CuO/CNT + h\nu \rightarrow e^- + h^+ \tag{5}$$

Due to the black color of all catalysts, their band gap energy could not be determined, however, based on the literature; the band gap of CuO is in the range of 1.2–1.5 eV [24]. As detected by the XPS, Raman and ESR analyses, the presence of surface defects (SD) and V$_o$ on both CuO and CNT between their VB and CB also allowed photooxidation to be carried out in the visible light region (Fig. 6). The electron excitation from the VB to SD and V$_o$ and from those levels to the CB led to generation of more electron–hole pairs. The e$^-$ subsequently reduced the O$_2$ to form superoxide radical anions •O$_2^-$ (Eq. (6)), which were then further reduced to form the active species •OH$_{bulk}$ (Eqs. (7)–(9)) to degrade the PCA which were already adsorbed on the surface of the catalyst (Eq. (10)):

$$e^- + O_2 \rightarrow {}^\bullet O_2^- \tag{6}$$

$${}^\bullet O_2^- + H^+ \rightarrow {}^\bullet HO_2 \tag{7}$$

$${}^\bullet HO_2 + H^+ + e^- \rightarrow H_2O_2 \tag{8}$$

$$H_2O_2 + e^- \rightarrow {}^\bullet OH_{bulk} + OH^- \tag{9}$$

$${}^\bullet OH_{bulk} + PCA \rightarrow \text{degraded product} \tag{10}$$

Table 4
Kinetics parameters for photodegradation of PCA over 50 wt% CuO/CNT catalyst.

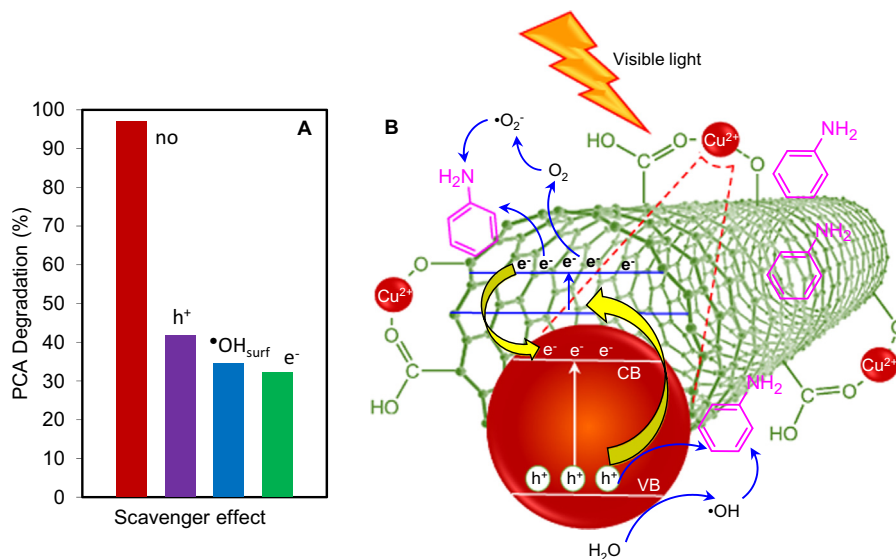| Initial Conc. C_0 (mg L^{-1})	$k \times 10^{-3}$ (min^{-1})	R^2	r_0 (mg L^{-1} min^{-1})
10	22.0	0.996	0.22
30	12.1	0.994	0.36
50	9.10	0.994	0.46
70	6.97	0.990	0.49
80	5.90	0.990	0.47
100	4.92	0.990	0.49

Fig. 6. (A) Scavenger effect on the 50 wt% CuO/CNT for PCA degradation (B) proposed mechanism for photodegradation of PCA.

The h^+ then reacted with the surface–adsorbed hydroxyl groups (OH^-) from water to yield $\cdot OH_{surf}$, which afterward degraded the PCA (Eq. (11)). In addition, the h^+ also triggered direct oxidation of the PCA to form reactive intermediates (Eq. (12)).

$$h^+ \;+\; OH^- \;\rightarrow\; \cdot OH_{surf} \tag{11}$$

$$h^+ \;+\; PCA \;\rightarrow\; \text{oxidized PCA} \tag{12}$$

The e^- generated at the CB of CNT were able to migrate to the CuO phase, due to the lower VB edge potentials of CuO as compared to CNT. In addition, the photogenerated holes on the VB of CuO could transfer easily to the CNT through the heterojunctions, since the VB edge potential of CuO is more positive than the LUMO of the CNT [28]. As a result, the electron–hole pair recombination rate could be reduced, and the synergistic effects given by both CuO and CNT significantly enhanced this adsorption-oriented photodegradation of PCA.

3.5. Mineralization, biodegradability, stability and other potential applications

The degree of mineralization during photocatalytic degradation of PCA was determined via total organic carbon (TOC) and biological oxygen demand (BOD_5) analyses in order to confirm whether the final solution of PCA was less toxic than the initial solution. In Fig. 7A, it was observed that after 3 h irradiation, the TOC value decreased to 89.1%, signifying the degradation of organic materials [59]. A significant change in BOD_5 (50.7%) demonstrated that this photo–oxidation system could enhance the biodegradability of the PCA solution by converting the non-biodegradable organics into biodegradable forms [60].

The potential of catalyst to be reused or recovered in photocatalytic processes is a great concern since it can contribute to lowering the operational cost of processes, thus making photocatalysis an attractive method for wastewater treatment [61]. Therefore, a repeated experiment was carried out using the 50 wt% CuO/CNT catalyst to study the stability of the catalyst during the degradation of PCA (Fig. 7B). It was
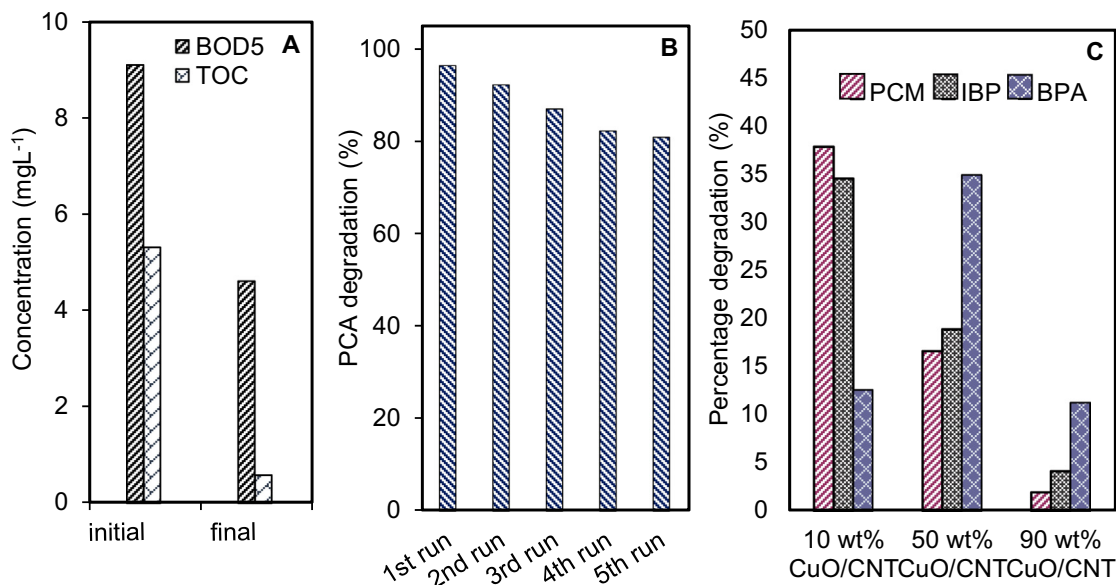

Fig. 7. (A) TOC and BOD_5 values before and after PCA degradation (B) recycling test for PCA degradation over 50 wt% CuO/CNT and (C) application on other type of endocrine disruption compounds.

Table 5
Comparison of CNT based photocatalyst for degradation of organic pollutants.

Catalyst	Target compound	Catalyst dosage (g L^{-1})	Initial conc. (mg L^{-1})	Degradation (%)	Ref.
TiO$_2$/CNT	Sudan(I)	0.5	10	>95	[62]
TiO$_2$/CNT	2,4-Dinitrophenol	8	38.8	>95	[63]
ZnO/CNT	Methyl Orange	0.3	20	>75	[64]
ZnO/CNT	Acetaldehyde	0.001	100	89	[65]
SnO$_2$/CNT	Rhodamine B	1	4.75	96	[66]
CuO/CNT	Direct Red 31	6.25	50	89	[67]
	Reactive Red 120			87	
Cu$_x$O–CNTs	Methyl Orange	0.0667	20	40	[68]
CuO/CNT	p-Nitrophenol	0.002	50	70	[69]
CuO/CNT	p-Chloroaniline	0.375	10	96	This study

observed that the 50 wt% CuO/CNT catalyst remained active even after five cycles, with just a slight decrease in the degradation percentage. The decrease in photocatalytic efficiency might be due to the heat treatment, which caused aggregation of the catalysts, thus decreasing their surface area. Hence, this proved the stability of 50 wt% CuO/CNT photocatalyst which not being easily deactivated during the degradation process.

The capability of the photocatalysts was also examined in the degradation of various endocrine disruption compound (EDCs) such as paracetamol (PCM), ibuprofen (IBP), and bisphenol A (BPA), and the results are shown in Fig. 7C. It was observed that the catalysts have great potential to be applied to various types of organic pollutants. EDCs are trace organic contaminants that have been detected in aquatic environments. They can mimic or antagonize natural hormones, hinder metabolic processes, occupy hormone receptors, and cause reproductive and developmental problems when consumed by humans and aquatic species.

For practical consideration, the performance of CuO/CNT was compared with various previous photocatalysts as listed in Table 5. It was observed that the efficiency of degradation of PCA carried out over CuO/CNT in this study was quite comparable with the degradation of both dyes and organic pollutants over various CNT based photocatalysts such as TiO$_2$/CNT, ZnO/CNT, SnO$_2$/CNT, and CuO/CNT. It could not be neglected that besides the reaction conditions, the degradation performance of each targeted reactant also depends on the functional groups attached to the aromatics as well as their position.

4. Conclusion

In summary, a full range of CuO/CNT catalysts were synthesized by electrolysis technique and their physicochemical properties were studied by XRD, N$_2$ adsorption-desorption, FTIR, XPS, Raman, and ESR. The XRD results showed that a lower amount of CuO was well distributed on the CNT, while higher amounts of CuO loading were agglomerated, hence lowered the specific surface area. The crystallite size of CuO seemed to increase with increasing CuO content, later blocking the pores of the CNTs. From the FTIR results, bands corresponding Cu—O—C bonds were found at 512 cm^{-1}, confirming the interaction between CuO and CNT. The Raman and ESR analyses verified the presence of surface defects and V$_o$. From adsorption studies, Langmuir isotherm model was fitted well, signifying the monolayer adsorption of the PCA at the outer surface of CuO/CNT. Moreover, from the Freundlich isotherm model, it was confirmed that the adsorption nature was chemisorption, where the C-N moieties from PCA adsorbed on the CuO/CNT catalyst. This shows the significant role played by the chemisorption process prior to photodegradation. The 50 wt% CuO/CNT which possessed the greatest numbers of Cu—O—C bonds, resulted in the highest degradation of 10 mg L^{-1} PCA (97%) within 3 h of reaction under visible light irradiation at 27 °C and neutral pH. Likewise, the kinetic of the photodegradation correlated with pseudo-first-order Langmuir–Hinshelwood model also verified the significance of the adsorption

in this photodegradation. The results of the effect of scavengers revealed that the photogenerated electron was the key factor in the photodegradation, followed by •OH$_{surf}$, and holes. The surface defects and V$_o$ played important roles in narrowing the band gap of the catalysts, as did electron capturers in hindering the electron–hole recombination and enhancing this visible–light–responsive–photodegradation. In addition, the reusability test revealed that the catalyst was still stable even after five cycles. Mineralization of PCA by TOC and BOD$_5$ analyses after 3 h of contact time were 89.1% and 50.7% respectively, demonstrating the prospective biodegradability of the PCA solution using this system. It was also noted that the CuO/CNT catalyst shows good potential in the degradation of various endocrine disruption compounds (EDCs).

Appendix A. Supplementary data

Supplementary data to this article can be found online at https://doi.org/10.1016/j.powtec.2017.12.052.

References

[1] Y. Zhang, H.P. Tran, X. Du, I. Hussain, S. Huang, S. Zhou, W. Wen, Efficient pyrite activating persulfate process for degradation of p-chloroaniline in aqueous systems: a mechanistic study, Chem. Eng. J. 308 (2017) 1112–1119.
[2] X. Du, Y. Zhang, I. Hussain, S. Huang, W. Huang, Insight into reactive oxygen species in persulfate activation with copper oxide: activated persulfate and trace radicals, Chem. Eng. J. 313 (2017) 1023–1032.
[3] I. Hussain, Y. Zhang, S. Huang, X. Du, Degradation of p-chloroaniline by persulfate activated with zero-valent iron, Chem. Eng. J. 203 (2012) 269–276.
[4] L. Zhu, Y. Yu, X. Xu, Z. Tian, W. Luo, High-rate biodegradation and metabolic pathways of 4-chloroaniline by aerobic granules, Process Biochem. 46 (2011) 894–899.
[5] L.L. Zhang, D. He, J.M. Chen, Y. Liu, Biodegradation of 2-chloroaniline, 3-chloroaniline, and 4-chloroaniline by a novel strain Delftia tsuruhatensis H1, J. Hazard. Mater. 179 (2010) 875–882.
[6] M. Sanchez, H. Wolfger, N. Getoff, Radiation-induced degradation of 4-chloroaniline in aqueous solution, Radiat. Phys. Chem. 65 (2002) 611–620.
[7] Y.P. Chang, C.L. Ren, J.C. Qu, X.G. Chen, Preparation and characterization of Fe3O4/graphene nanocomposites and investigation of its adsorption performance for aniline and p-chloroaniline, Appl. Surf. Sci. 261 (2012) 504–509.
[8] S. Andini, R. Cioffi, F. Colangelo, F. Montagnaro, L. Santoro, Adsorption of chlorophenol, chloroaniline and methylene blue on fuel oil fly ash, J. Hazrd. Mater. 157 (2008) 599–604.
[9] S. Selvarajan, P. Malathy, A. Suganthi, M. Rajarajan, Fabrication of mesoporous BaTiO3/SnO2 nanorods with highly enhanced photocatalytic degradation of organic pollutants, J. Ind. Eng. Chem. 53 (2017) 201–212.
[10] A. Gil, A.M. García, M. Fernández, M.A. Vicente, B. González-Rodríguez, V. Rives, S.A. Korili, Effect of dopants on the structure of titanium oxide used as a photocatalyst for the removal of emergent contaminants, J. Ind. Eng. Chem. 53 (2017) 183–191.
[11] H. Derikvandi, A. Nezamzadeh-Ejhieh, Comprehensive study on enhanced photocatalytic activity of heterojunction ZnS-NiS/zeolite nanoparticles: experimental design based on response surface methodology (RSM), impedance spectroscopy and GC-MASS studies, J. Colloid Interface Sci. 490 (2017) 652–664.
[12] V.K. Gupta, R. Saravanan, S. Agarwal, F. Gracia, M.M. Khan, J. Qin, R.V. Mangalaraja, Degradation of azo dyes under different wavelengths of UV light with chitosan-SnO2 nanocomposites, J. Mol. Liq. 232 (2017) 423–430.
[13] J. Qin, C. Yang, M. Cao, X. Zhang, S. Rajendran, S. Limpanart, M. Mingzhen, R. Liu, Two-dimensional porous sheet-like carbon-doped ZnO/gC3N4 nanocomposite with high visible-light photocatalytic performance, Mater. Lett. 189 (2017) 156–159.
[14] G.J. Lee, J.J. Wu, Recent developments in ZnS photocatalysts from synthesis to photocatalytic applications-a review, Powder Technol. 318 (2017) 8–22.
[15] N.W.C. Jusoh, A.A. Jalil, S. Triwahyono, A.H. Karim, N.F. Salleh, N.H.R. Annuar, N.F. Jaafar, M.L. Firmansyah, R.R. Mukti, M.W. Ali, Structural rearrangement of mesostructured silica nanoparticles incorporated with ZnO catalyst and its photoactivities: effect of alkaline aqueous electrolyte concentration, Appl. Surf. Sci. 330 (2015) 10–19.
[16] L. Gnanasekaran, R. Hemamalini, R. Saravanan, K. Ravichandran, F. Gracia, S. Agarwal, V.K. Gupta, Synthesis and characterization of metal oxides (CeO2, CuO, NiO, Mn3O4, SnO2 and ZnO) nanoparticles as photo catalysts for degradation of textile dyes, J. Photochem. Photobiol. B 173 (2017) 43–49.
[17] R. Verma, A. Awasthi, P. Singh, R. Srivastava, H. Sheng, J. Wen, D.J. Miller, A.K. Srivastava, Interactions of titania based nanoparticles with silica and green-tea: photo-degradation and-luminescence, J. Colloid Interface Sci. 475 (2016) 82–95.

[18] I. Janson, K. Kobayashi, H. Hori, B. Sanchez, B. Ohtani, S. Suarez, Decahedral anatase titania particles immobilized on zeolitic materials for photocatalytic degradation of VOC, Catal. Today 207 (2017) 22–29.

[19] M. Romero-Sáez, L.Y. Jaramillo, R. Saravanan, N. Benito, E. Pabón, E. Mosquera, F. Gracia, Notable photocatalytic activity of TiO2-polyethylene nanocomposites for visible light degradation of organic pollutants, Express Polym Lett 11 (2017) 899–909.

[20] S. He, Y. Hu, J. Wan, Q. Gao, Y. Wang, S. Xie, L. Qiu, C. Wang, G. Zheng, B. Wang, H. Peng, Biocompatible carbon nanotube fibers for implantable supercapacitors, Carbon 122 (2017) 162–167.

[21] S. Mallakpur, E. Khadem, Carbon nanotube-metal oxide nanocomposites: fabrication, properties and applications, Chem. Eng. J. 302 (2016) 344–367.

[22] A. Bazargan, G. McKay, A review-synthesis of carbon nanotubes from plastic wastes, Chem. Eng. J. 195-196 (2012) 377–391.

[23] C.H. See, A.T. Harris, A review of carbon nanotube synthesis via fluidize-bed chemical vapor deposition, Ind. Eng. Chem. Res. 46 (2007) 997–1012.

[24] T. Pandiyarajan, R. Saravanan, B. Karthikeyan, F. Gracia, H.D. Mansilla, M.A. Gracia-Pinilla, R.V. Mangalaraja, Sonochemical synthesis of CuO nanostructures and their morphology dependent optical and visible light driven photocatalytic properties, J. Mater. Sci. Mater. Electron. 28 (3) (2017) 2448–2457.

[25] G. Mailhot, L. Hykrdova, J. Jirkovsky, K. Lemr, G. Grabner, M. Bolte, Iron (III)-photoinduced degradation of 4-chloroaniline in aqueous solution, Appl. Catal. B Environ. 50 (2004) 25–35.

[26] H.Y. Liang, Y.Q. Zhang, S.B. Huang, I. Hussain, Oxidative degradation of p-chloroaniline by copper oxidate activated persulfate, Chem. Eng. J. 218 (2013) 384–391.

[27] A.A. Jalil, N.F.A. Panjang, S. Akhbar, M. Sundang, N. Tajuddin, S. Triwahyono, Complete electrochemical dechlorination of chlorobenzenes in the presence of naphthalene mediator, J. Hazard. Mater. 148 (2007) 1–5.

[28] N.F. Khusnun, A.A. Jalil, S. Triwahyono, N.W.C. Jusoh, A. Johari, K. Kidam, Interaction between copper and carbon nanotubes triggers their mutual role in the enhanced photodegradation of p-chloroaniline, Phys. Chem. Chem. Phys. 18 (2016) 12323–12331.

[29] C.N.C. Hitam, A.A. Jalil, S. Triwahyono, A. Ahmad, N.F. Jaafar, N. Salamun, N.A.A. Fatah, L.P. Teh, N.F. Khusnun, Z. Ghazali, Synergistic interaction of Cu and N on surface altered amorphous TiO2 nanoparticles for enhanced photocatalytic oxidative desulfurization of dibenzothiophane, RSC Adv. 6 (2016) 76259–76268.

[30] M. Liu, X. Ding, Q. Yang, Y. Wang, G. Zhao, N. Yang, A pM leveled photoelectrochemical sensor for microcystin-LR based on surface molecularly imprinted TiO2@CNT nanostructure, J. Hazard. Mater. 331 (2017) 309–320.

[31] R. Jusoh, A.A. Jalil, S. Triwahyono, A. Idris, M.Y. Noordin, Photodegradation of 2-chlorophenol over colloidal a-FeOOH supported mesostructured silica nanoparticles: influence of a pore expander and reaction optimization, Sep. Purif.Technol. 149 (2015) 55–64.

[32] G. Sheng, A. Alsaedi, W. Shammakh, S. Monaquel, J. Sheng, X. Wang, H. Li, Y. Huang, Enhanced sequestration of selenite in water by nanoscale zero valent iron immobilization on carbon nanotubes by a combined batch, XPS and XAFS investigation, Carbon 99 (2016) 123–130.

[33] S. Joshi, S.J. Ippolito, M.V. Sunkara, Convinient architectures of Cu2O/SnO2 type II p-n heterojunctions and their application in visible light catalytic degradation of rhodamine B, RSC Adv. 6 (2016) 43672–43684.

[34] F. Li, Y. Wang, D. Wang, F. Wei, Characterization of single walled carbon nanotubes by N2 adsorption, Carbon 42 (2004) 2375–2383.

[35] J. Landers, G.Y. Gor, A.V. Neimark, Density functional theory methods for characterization of porous materials, Colloids Surf. A 437 (2013) 3–32.

[36] N.F. Jaafar, A.A. Jalil, S. Triwahyono, N. Shamsuddin, New insight into self-modification of mesoporous titania nanoparticles for enhanced photoactivity: effect of microwave power density on formation of oxygen vacancies and Ti 3+, RSC Adv. 5 (2015) 90991–91000.

[37] A.H. Karim, A.A. Jalil, S. Triwahyono, N.H.N. Kamarudin, A. Ripin, Influence of multi-walled carbon nanotubes on textural and adsorption characteristics of in situ synthesized mesostructured silica, J. Colloid Interface Sci. 421 (2014) 93–102.

[38] J. Matos, S. Miralles-Cuevas, A. Ruíz-Delgado, I. Oller, S. Malato, Development of TiO2-C photocatalysts for solar treatment of polluted water, Carbon 122 (2017) 361–373.

[39] G. Kliche, Z.V. Popovic, Far-infrared spectroscopic investigations on CuO, Phys. Rev. B 42 (1990) 10060–10066.

[40] A.S. Ethiraj, D.J. Kang, Synthesis and characterization of CuO nanowires by a simple wet chemical method, Nanoscale Res. Lett. 7 (2012) 70.

[41] O.E. Fayemi, A.S. Adekunle, E.E. Ebenso, Metal oxide nanoparticles/multi-walled carbon nanotube nanocomposite modified electrode for the detection of dopamine: comparative electrochemical study, J. Biosens. Bioelectron. 6 (2015) 190.

[42] M. Chipara, J.M. Zaleski, D. Hui, C. Du, N. Pan, Electron spin resonance on carbon nanotubes-polymer composites, J. Polym. Sci. B 43 (34) (2005) 6–3412.

[43] D.K. Singh, P.K. Iyer, P.K. Giri, Optical signature of structural defects in single and multiwalled carbon nanotubes, J. Nanosci. Nanotechnol. 9 (2009) 1–6.

[44] A.V. Sidorenko, P.A. Rodnyi, O. Guillot-Noel, D. Gourier, C.W.E. van Eijk, Study of ESR spectra of Ce 3+ ions in polycrystalline Sr2B5O9Br, Phys. Solid State 45 (2003) 1376–1678.

[45] A. Viano, S.R. Mishra, R. Lloyd, J. Losby, T. Gheyi, Thermal effects on ESR signal evolution in nano and bulk CuO powder, J. Non-Cryst. Solids 325 (2003) 16–21.

[46] J. Loubser, J. van Wyk, Electron spin resonance in the study of diamond, Rep. Prog. Phys. 41 (1978) 1201–1245.

[47] C.C. Hsieh, W.R. Liu, Synthesis and characterization of nitrogen-doped graphene nanosheets/copper composite film for thermal dissipation, Carbon 118 (2017) 1–7.

[48] M. Arjmand, K. Chizari, B. Krause, P. Poetschke, U. Sundararaj, Effect of synthesis catalyst on structure of nitrogen-doped carbon nanotubes and electrical conductivity and electromagnetic interference shielding of their polymeric nanocomposites, Carbon 98 (2016) 358–372.

[49] A.A. Dubale, C.J. Pan, A.G. Tamirat, H.M. Chen, W.N. Su, C.H. Chen, J. Rick, D.W. Ayele, B.A. Aragaw, J.F. Lee, Y.W. Yang, Heterostructured Cu2O/CuO decorated with nickel as a highly efficient photocathode for photoelectrochemical water reduction, J. Mater. Chem. A 3 (2015) 12482–12499.

[50] N. Salamun, S. Triwahyono, A.A. Jalil, T. Matsuura, N.F.M. Salleh, Acid-vacuo heat treated low cost banana stems fiber for efficient biosorption of Hg(II), RSC Adv. 5 (2015) (14129-12137).

[51] N.F.M. Salleh, A.A. Jalil, S. Triwahyono, J. Efendi, R.R. Mukti, B.H. Hameed, New insight into electrochemical-induced synthesis of NiAl2O4/Al2O3: synergistic effect of surface hydroxyl groups and magnetism for enhanced adsorptivity of Pd (II), Appl. Surf. Sci. 349 (2015) 485–495.

[52] M. Mihaylov, S. Andonova, K. Chakarova, A. Vimint, E. Ivanova, N. Drenchev, K. Hadjivanov, An advanced approach for measuring acidity of hydroxyls in confined space: FTIR study of low-temperature CO and 15N2 adsorption on MOF samples from the MIL-53(Al) series, Phys. Chem. Chem. Phys. 17 (2015) 24304–24314.

[53] N.G. Asenjo, R. Santamaría, C. Blanco, M. Granda, P. Álvarez, R. Menéndez, Correct use of the Langmuir–Hinshelwood equation for proving the absence of a synergy effect in the photocatalytic degradation of phenol on a suspended mixture of titania and activated carbon, Carbon 55 (2013) 62–69.

[54] A.H.A. Rahman, C.L. Teo, A. Idris, E. Misran, S.A.N. Leong, Polyvinyl alcohol–alginate ferrophoto gels for mercury (II) removal, J. Ind. Eng. Chem. 33 (2016) 190–196.

[55] J. Feng, Y. Hou, X. Wang, W. Quan, J. Zhang, Y. Wang, L. Li, In-depth study on adsorption and photocatalytic performance of novel reduced graphene oxide- ZnFe2O4-polyaniline composites, J. Alloys Compd. 681 (2016) 157–166.

[56] J. Shen, G. Ma, J. Zhang, W. Quan, L. Li, Facile fabrication of magnetic reduced graphene oxide-ZnFe2O4 composites with enhanced adsorption and photocatalytic activity, Appl. Surf. Sci. 359 (2015) 455–468.

[57] H. Li, Z. Su, S. Hu, Y. Yan, Free standing and flexible Cu/Cu2O/CuO heteroj0unction net: a novel material as cost-effective and easily recycled visible-light photocatalyst, Appl. Catal. B Environ. 207 (2017) 134–142.

[58] Y. Ma, N. Lu, Y. Lu, J.N. Guan, J. Qu, H.Y. Liu, Q. Chong, X. Yuan, Comparative study of carbon materials synthesized "greenly" for 2-CP removal, Sci. Rep. 6 (2016)https://doi.org/10.1038/srep29167.

[59] A.F.A. Rahman, A.A. Jalil, S. Triwahyono, A. Ripin, F.F.A. Aziz, N.A.A. Fatah, N.F. Jaafar, C.N.C. Hitam, N.F.M. Salleh, N.S. Hassan, Strategies for introducing titania onto mesostructured silica nanoparticle targeting enhanced photocatalytic activity of visible-light-responsive Ti-MSN catalysts, J. Clean. Prod. 143 (2017) 948–959.

[60] V. Romere, N. De la Cruz, R.F. Dantas, P. Marco, J. Jimenez, S. Esplugas, Photocatalytic treatment of metoprolol and propranolol, Catal. Today 161 (2011) 115–120.

[61] F.H. Mustapha, A.A. Jalil, M. Mohamed, S. Triwahyono, N.S. Hassan, N.F. Khusnun, C.N.C. Hitam, A.F.A. Rahman, L. Firmanshah, A.S. Zolkifli, New insight into self-modified surfaces with defect-rich rutile TiO2 as a visible-light-driven photocatalyst, J. Clean. Prod. 168 (2017) 1150–1162.

[62] A. Miribangul, X. Ma, C. Zeng, H. Zou, Y. Wu, T. Fan, Z. Su, Synthesis of TiO2/CNT composites and its photocatalytic activity toward Sudan (I) degradation, Photochem. Photbiol. 92 (4) (2016) 523–527.

[63] H. Wang, H.L. Wang, W.F. Jiang, Z.Q. Li, Photocatalytic degradation of 2,4-dinitrophenol (DNP) by multi-walled carbon nanotubes (MWCNTs)/TiO2 composite in aqueous solution under solar irradiation, Water Res. 43 (1) (2009) 204–210.

[64] X. Wang, S. Yao, X. Li, Sol-gel preparation of CNT/ZnO nanocomposite and its photocatalytic property, Chin. J. Chem. 27 (7) (2009) 1317–1320.

[65] T.A. Saleh, M.A. Gondal, Q.A. Drmosh, Z.H. Yamani, A. Al-Yamani, Enhancement in photocatalytic activity for acetaldehyde removal by embedding ZnO nano particles on multiwall carbon nanotubes, Chem. Eng. J. 166 (1) (2011) 407–412.

[66] S. Wu, W. Dai, Microwave-hydrothermal synthesis of SnO2-CNTs hybrid nanocomposites with visible light photocatalytic activity, Nano 7 (3) (2017) 54.

[67] N.M. Mahmoodi, P. Rezaei, C. Ghotbei, M. Kazemeini, Copper oxide-carbon nanotube (CuO/CNT) nanocomposite: synthesis and photocatalytic dye degradation from colored textile wastewater, Fibers Polym. 17 (11) (2016) 1842–1848.

[68] B. Zeng, X. Chen, X. Ning, C. Chen, A. Hu, W. Deng, CNTs/rGO spheres decorated with Cu x O (x = 1 or 2) nanoparticles and its photocatalytic performance, Catal. Commun. 43 (2014) 235–239.

[69] L.B. Liu, S. Qin, J.J. Wang, W.J. Zheng, X.W. Du, Photothermal synthesis of ultrafine CuxO nanoparticles on carbon nanotubes for photosensitized degradation, Chem. Commun. 51 (26) (2015) 5660–5663.